ADVANCED MATERIALS
www.advmat.de

A Soft-Fiber Bioelectronic Device with Axon-Like Architecture Enables Reliable Neural Recording In Vivo under Vigorous Activities

Chengqiang Tang, Zhengqi Han, Ziwei Liu, Wenjun Li, Jiahao Shen, Kailin Zhang, Shuting Mai, Jinyan Li, Xiao Sun, Xingfei Chen, Hongjian Li, Liyuan Wang, Jiaheng Liang, Meng Liao, Jianyou Feng, Chuang Wang, Jiajia Wang, Lei Ye, Yiqing Yang, Songlin Xie, Xiang Shi, Kaiwen Zeng, Xuefeng Zhang, Xiangran Cheng, Kun Zhang, Yue Guo, Han Yang, Yifei Xu, Qi Tong, Hongbo Yu, Peining Chen, Huisheng Peng,* and Xuemei Sun**

Implantable neural devices that record neurons in various states, including static states, light activities such as walking, and vigorous activities such as running, offer opportunities for understanding brain functions and dysfunctions. However, recording neurons under vigorous activities remains a long-standing challenge because it leads to intense brain deformation. Thus, three key requirements are needed simultaneously for neural devices, that is, low modulus, low specific interfacial impedance, and high electrical conductivity, to realize stable device/brain interfaces and high-quality transmission of neural signals. However, they always contradict each other in current material strategies. Here, a soft fiber neural device capable of stably tracking individual neurons in the deep brain of medium-sized animals under vigorous activity is reported. Inspired by the axon architecture, this fiber neural device is constructed with a conductive gel fiber possessing a network-in-liquid structure using conjugated polymers and liquid matrices and then insulated with soft fluorine rubber. This strategy reconciles the contradictions and simultaneously confers the fiber neural device with low modulus (300 kPa), low specific impedance (579 kΩ μm^2), and high electrical conductivity (32 700 S m^{-1}) – ≈1–3 times higher than hydrogels. Stable single-unit spike tracking in running cats, which promises new opportunities for neuroscience is demonstrated.

1. Introduction

We strive to understand the human and animal brains, in terms of vision production, perception, consciousness, and action, when they are under indispensable states, including static states, light activities like walking, and vigorous activities such as running and hopping in normal lives.[1] Although several pioneering studies have performed neural recording under static states and light activities,[2] it remains challenging to realize stable neural recording (e.g., single-unit tracking) in the deep brain under vigorous activities such as running without head fixation, especially in medium-sized and large animals.[3]

For the aforementioned neural devices, the relative motion between the devices and tissues occurs dynamically, causing brain damage and signal loss. To address this issue, these devices have evolved from being rigid to flexible to achieve mechanical matching with brain tissues.[4] Flexibility was mainly realized using a

C. Tang, Z. Liu, W. Li, K. Zhang, S. Mai, J. Li, X. Sun, L. Wang, M. Liao, J. Feng, C. Wang, J. Wang, L. Ye, Y. Yang, S. Xie, X. Shi, K. Zeng, X. Cheng, K. Zhang, Y. Guo, H. Yang, Y. Xu, P. Chen, H. Peng, X. Sun
State Key Laboratory of Molecular Engineering of Polymers
Department of Macromolecular Science
Institute of Fiber Materials and Devices
and Laboratory of Advanced Materials
Fudan University
Shanghai 200438, China
E-mail: penghs@fudan.edu.cn; sunxm@fudan.edu.cn

The ORCID identification number(s) for the author(s) of this article can be found under https://doi.org/10.1002/adma.202407874

DOI: 10.1002/adma.202407874

Z. Han, X. Chen, H. Li, J. Liang, H. Yu
Vision Research Laboratory
School of Life Sciences
State Key Laboratory of Medical Neurobiology
and Collaborative Innovation Center for Brain Science
Fudan University
Shanghai 200438, China
E-mail: hongboyu@fudan.edu.cn

J. Shen, Q. Tong
Department of Aeronautics and Astronautics
Fudan University
Shanghai 200433, China

non-stretchable, high-modulus polymer substrate such as SU-8 and by reducing the device size to decrease the bending stiffness in the lateral direction. Although these flexible devices could obtain stable neural recordings when animals are in static and freely moving states,[5] particularly for small animals such as mice and rats, achieving the same under vigorous activities in larger animals is challenging. In larger animals, more severe dynamic deformations of brain tissues occur in three dimensions, thus placing much higher demands on neural devices. For instance, the maximum deformation in the mouse brain is approximately in the range of tens of micrometers, while it can reach up to 4 mm in the human brain.[6] Therefore, axially stretchable devices with low intrinsic moduli are required to match these large brain deformations. Although conductive filler-blended elastomers[7] and hydrogels[8] have been explored to have low modulus and stretchability, their high specific impedances ($>10^{10}$ kΩ μm^2 for elastomers and $>10^6$ kΩ μm^{-2} for hydrogels) and low electrical conductivities ($<10^{-4}$ S m^{-1} for elastomers and <10 S m^{-1} for hydrogels) often failed to meet the requirements for high-fidelity neural signal transmission. Therefore, there is an urgent need for new materials and structural designs for neural devices that simultaneously exhibit intrinsically low moduli, low specific impedances, and high electrical conductivity to accommodate large brain deformations and realize stable neural recordings under vigorous activities in animals larger than mice and rats.

Herein, we report a soft-fiber neural device (FND) to address the aforementioned challenges and demonstrate stable single-unit spike tracking in the brain of the cat, a medium-sized animal, even during running. Inspired by the unique structure of axons, in which flexibility is derived from networks of thin neurofilaments confined in a liquid-rich axoplasm (**Figure 1a**),[9] we designed a similar network-in-liquid structure for our FND (Figure 1b). In axons, the structure composed of neurofilament proteins and α-internexin,[10] which is entropically elastic, assisting neurons in maintaining their connections and transmit neural signals even under vigorous activities. In our gel fiber, we used poly(3,4 ethylenedioxythiophene): poly(styrenesulfonate) (PEDOT: PSS) as the building blocks of the conductive nanofiber network and a mixture of glycerol and water as the liquid matrix. PEDOT: PSS was selected because of its high conductivity and biocompatibility.[11] Fluorine rubber was used for insulation, similar to the myelin sheath, owing to its low modulus and ease of processing. Constructed with an axon-like architecture, our FND exhibited an ideal combination of the three requirements and successfully tracked single-unit spikes from individual neurons in the brain of a running cat. Overall, our study presents a general and effective strategy for designing high-performance neural devices capable of robust operation under complex conditions, thereby providing a valuable and reliable platform for brain studies.

X. Zhang
School of Life Sciences
Fudan University
Shanghai 200433, China

2. Results

2.1. Preparation and Characterization of FNDs

A standard wet-spinning process was used to produce the primary fibers for the gel fibers (Figure S1, Supporting Information). Briefly, the PEDOT: PSS solution was extruded into a mixture of isopropyl alcohol and dimethyl sulfoxide (DMSO) to obtain primary fibers, which were washed and dried before being infiltrated with a liquid matrix composed of glycerol and water. The gel fibers had smooth surfaces and a diameter of ≈15 μm (Figure 1c,d). Scanning electron microscopy (SEM) and transmission electron microscopy (TEM) images showed that the gel fibers were composed of entangled PEDOT: PSS nanofibers with a diameter of ≈60 nm. These nanofibers comprised intertwined bundles of smaller nanofibers with diameters of ≈5 nm (Figure 1e,f). The small-angle X-ray scattering pattern showed that the nanofibers in the gel fibers were isotropic (Figure S2, Supporting Information). Our gel fiber structure resembled the hierarchical organization of protein chains and α-internexin into protofilaments and neurofilaments. Furthermore, graph theory was used to quantitatively evaluate the nanofiber matrix of the gel fiber using the Structural GT software. Our gel fiber had a higher average nodal connectivity than some biological matrices such as the collagen matrix, indicating a higher robustness of the network in the gel fiber (Table S1, Supporting Information).[12] The FND was obtained after the gel fiber was insulated by fluorine rubber with a thickness of ≈1 μm (Figure 1g,h). These FNDs could be produced on a large scale with high consistency, enabling the use of multiple basic units to construct different types of neural devices, such as single-channel devices, tetrodes, and multichannel bundles with customized spatial distributions (Figure 1i; Figure S3, Supporting Information).

The gel fibers were flexible and exhibited a modulus in the kPa range (Movie S1, Supporting Information). This flexibility was attributed to the network-in-liquid structure, that allowed the nanofiber networks to deform freely in the large interspaces of the liquid matrix, similar to the behavior of neurofilaments in the axoplasm of axons.[10a,b] Finite-element simulations showed that when a network-in-liquid model was stretched, the network behaved like an elastic body (**Figure 2a**; Figure S4a, Supporting Information). The liquid matrix, which holds the network together, flows and follows the deformed network. Consequently, the effective modulus of the network-in-liquid model was primarily attributed to the nanofiber network occupying a small volume of the model. Furthermore, because most nanofibers in the network are curved and capable of deforming and recovering easily under an external force (i.e., entropically elastic), the moduli of the network-in-liquid models are typically several orders of magnitude lower than those of the condensed models (Figure S5, Supporting Information). The simulated moduli could also be further decreased by reducing the network density (Figure 2b; Figure S4b, Supporting Information).

Based on the simulation results, we increased the amount of filled liquid matrix to obtain low-modulus gel fibers containing stable and low-density networks. Because PEDOT is insoluble and hydrophobic,[13] the amount of liquid used depends on the difference between the solubility parameter for PSS (δ_{PSS}) and liquid matrix (δ_l) ($\delta_{PSS} - \delta_l$) (Discussion S1).

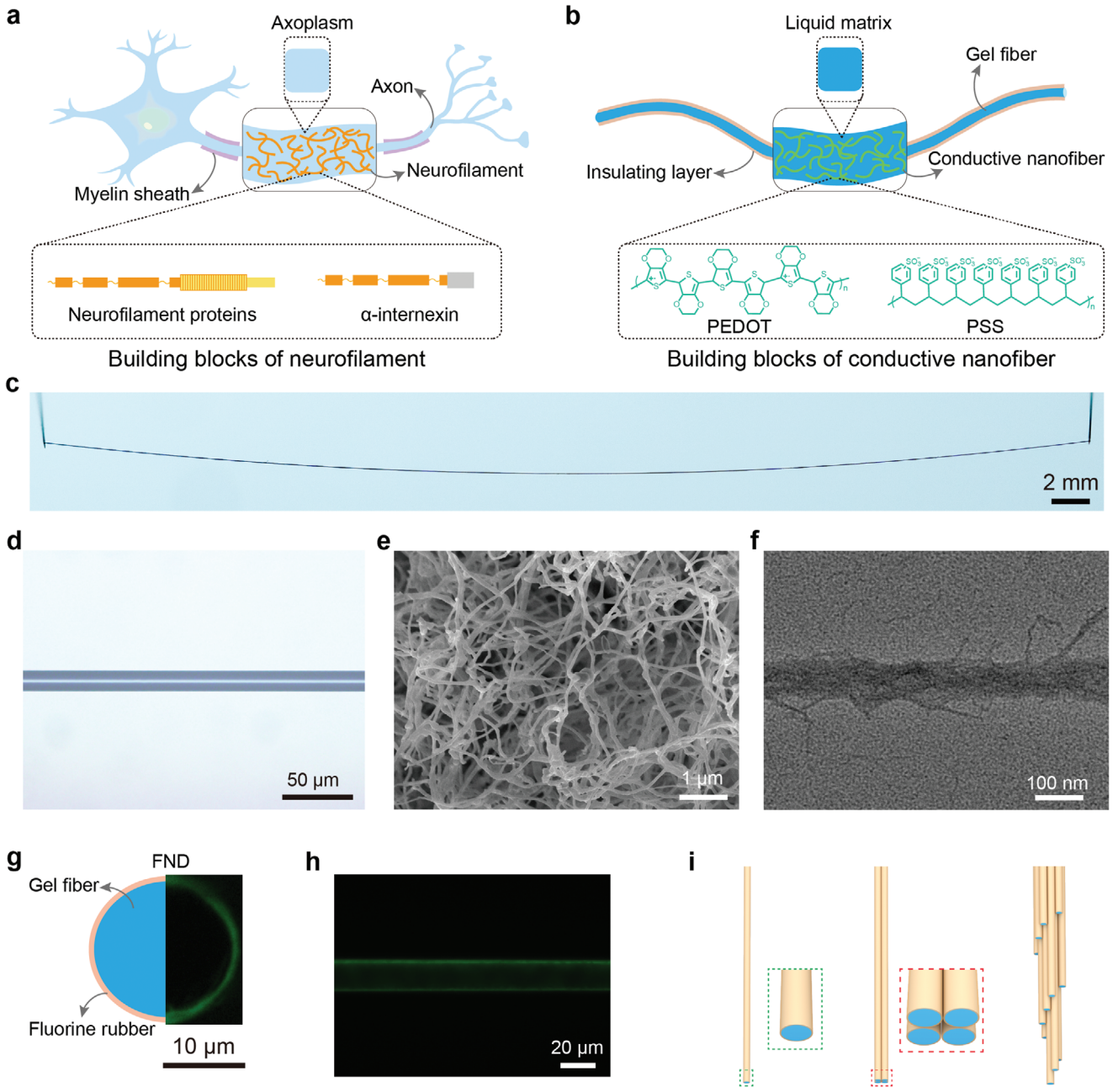

Figure 1. Design and structure of soft FNDs resembling axon skeleton. a,b) Schematic of network-in-liquid structure in neuron axon (a) and FND (b). PEDOT and PSS in our FND mimic the neurofilament proteins and α-internexin in axon neurofilaments. The liquid matrix representing axoplasm in our FND is a mixture of glycerol and water. c,d) Photograph and optical microscope image of a gel fiber with a diameter of ≈15 μm. e) SEM image showing that the gel fiber is composed of nanofiber networks. The sample was freeze-dried. f) TEM image showing a conductive nanofiber with a diameter of ≈60 nm, which is composed of smaller nanofibers with diameters of ≈5 nm. g) Cross-sectional image of the FND. Schematic (left) and fluorescence microscope images (right) are simultaneously used to show that the gel fiber is insulated with fluorine rubber. The thickness of the insulation layer is ≈1 μm. h) Fluorescence image of the side of the FND, showing that the fluorine rubber is evenly coated on the gel fiber. i) Schematic showing that the FNDs can be used as basic units to construct single-channel devices, tetrodes, and multichannel bundles with customized spatial distributions.

δ_l was tuned by varying the molar ratios of glycerol and water (Figure 2c). When the difference between δ_{PSS} and δ_l narrowed, the network density decreased, leading to lower modulus. The lowest modulus obtained for the gel fibers was 85 kPa (Figure 2d). Depending on the application, the modulus could be increased to 605 kPa or higher (Figures S4c,d,S6,S7, Supporting Information). For example, blood vessel applications require moduli > 100 kPa,[14] whereas for cartilage, the moduli of the fibers should be >500 kPa.[15]

In addition to the gel fiber, the insulating layer also impacts the properties of the FND. On the one hand, the insulating layer should be as thin as possible to reduce the overall size and

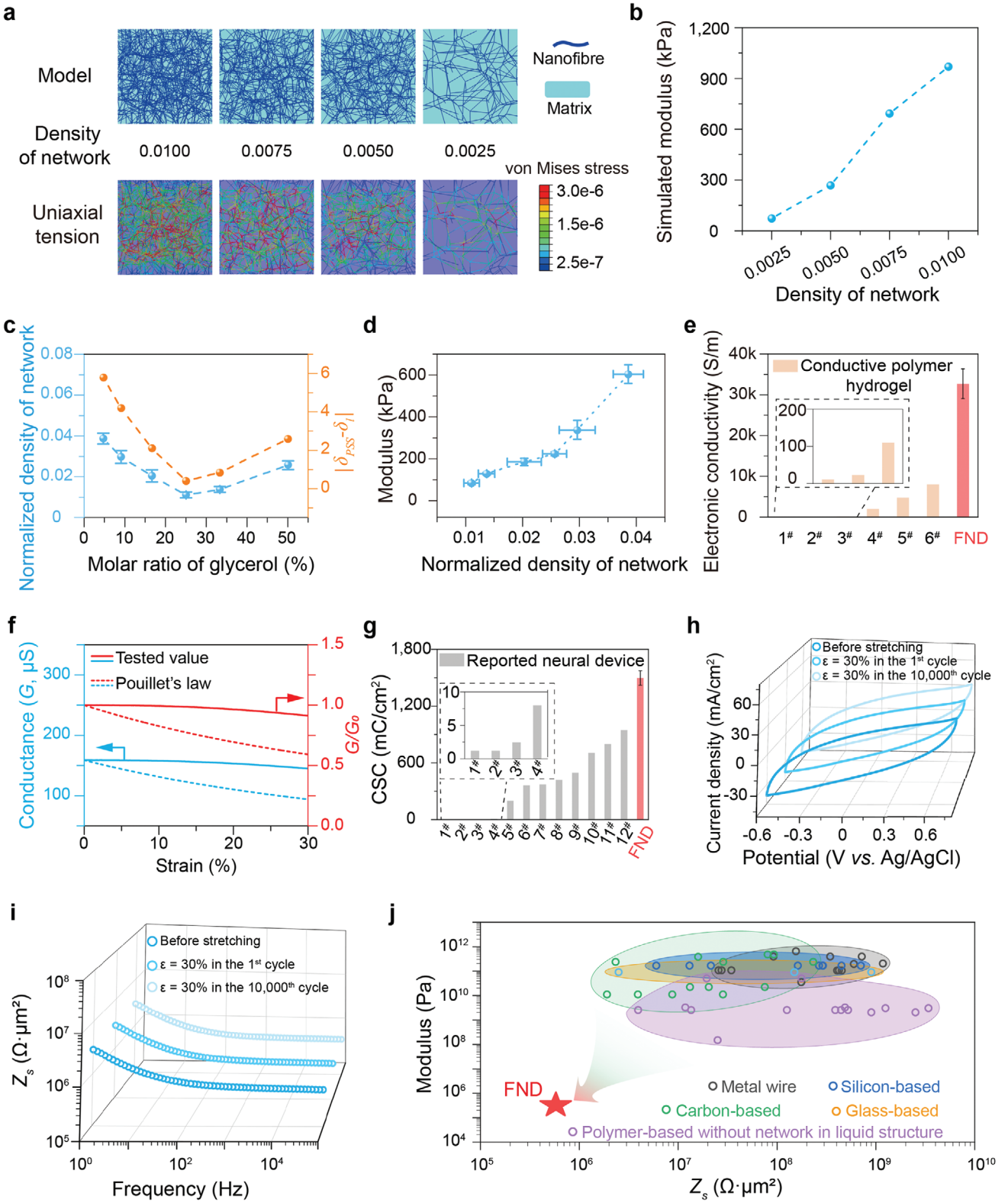

Figure 2. Mechanical and electrical performance of the FND. a) Finite-element simulations of network-in-liquid models under the same uniaxial tension show lower density network requires less stress. Top row: models with different densities of networks; bottom row: stress distributions in different models. b) Simulated moduli of network-in-liquid models in (a) show modulus can be tuned by changing the density of the network. c) Normalized density of the network (blue curve; each point is the average value measured from five samples) could be tuned by changing the absolute difference of δ_{PSS} and δ_l (yellow curve; theoretically calculated value). δ_{PSS} is the solubility parameter of PSS and δ_l is the solubility parameter of the liquid matrix,

modulus of the device. However, a sufficient thickness is required to prevent current leakage. Fluorine rubber was selected as the insulating layer because of its low modulus, high stretchability, and chemical resistance.[16] Fluorine rubber can also be dissolved in volatile solvents to prevent Plateau–Rayleigh instability during the coating.[17] This method tightly wraps the insulating layer around the gel fiber to prevent interface delamination (Figure S8, Supporting Information). The peeling test showed that the interface toughness between these two materials was 1.80 J m^{-2}, approximately one-third that of a commercial pressure-sensitive adhesive (Figure S9, Supporting Information).[18] The thickness of the fluorine rubber can be controlled by varying the concentration and coating speed according to the Landau–Levich law.[19] After optimization, a thickness of ≈1 μm was used, showing a leakage current at the pA level and a coupling capacitance between the conductive path and the surrounding medium at the pF level, which were comparable to the values of other neural devices (Figure S10a,b, Supporting Information).[20] With this thin insulating layer, the modulus of the FND was ≈300 kPa (Discussion S2, Figure S11, Supporting Information). In addition, the FND could also be stretched to more than 30% of its length while maintaining stable insulating performances (Figure S10c–e, Supporting Information).

In addition to the mechanical performance, the network-in-liquid structure endowed the FND with electrical conductivity (32 700 S m^{-1}), which was one to three orders of magnitude higher than that of many soft polymer hydrogels (Figure 2e; Figure S12a, Table S2, Supporting Information). Moreover, our FND was stretchable and exhibited only a 9% decrease in conductance at 30% elongation. This reduction was less than one-sixth of the value calculated using Pouillet's law, which is typically followed for common stretchable conductors, such as hydrogels and elastic composites (Figure 2f, Movie S2, Supporting Information).[21] This remarkable electrical performance is attributed to the network-in-liquid structure of the gel fibers. During stretching, adjacent nanofibers moved closer to form new conductive pathways, which would offset the attenuated conductance resulting from network damage (Discussion S3, Supporting Information).[22] This stable charge transfer under dynamic deformation is critical for maintaining stable neural recordings in vivo, as the brain undergoes dynamic changes, and deformations can exceed 25% strain under intense vigorous activities.[2b,4a,23]

The charge storage capacity (CSC) describes the amount of charge an electrode can transfer at the interface at a given potential. The CSC of our FND (1497 mC cm^{-2}) was the highest among other neural devices based on Pt wires (1.2 mC cm^{-2}), PtIr wires (8 mC cm^{-2}), carbon nanotube fibers (420 mC cm^{-2}), and graphene fibers (946 mC cm^{-2}) (Figure 2g; Figure S12b, Table S3, Supporting Information). Furthermore, CSC remained stable for over 10 000 stretching cycles at 30% strain (Figure 2h; Figure S12c, Supporting Information).

The impedance of a neural device, that indicates how well the device resists the charge flow of neural signals across the interface, typically increases with smaller device tips. To lower impedance, conventional metal and silicone devices are typically roughened or coated with nanomaterials to increase their surface area and capacitance.[24] In our FNDs, the intrinsic nanofiber network-in-liquid structure based on the conductive polymers of PEDOT: PSS provided both high surface area and capacitance, leading to a low specific impedance of 579 kΩ $μm^2$ (at 1 kHz). Consequently, FNDs can be very thin while maintaining a low impedance for effective neural recording.

Compared with conventional devices such as PtIr wires, whose specific impedance increases by several orders of magnitude as the frequency decreases from 1 MHz to 1 Hz, the specific impedance of the FND showed less variation. This stability is attributed to the conducting polymers, which facilitate intimate ion interactions and provide substantial capacitance (Figures S10b,S12d, Supporting Information).[25] The cut-off frequency of the FNDs was less than 1 Hz, as confirmed by the phase values above −45° across various frequencies (Figure S12e, Supporting Information). This electrical performance ensured the effective recording of neural signals from low-frequency local field potentials to high-frequency action potentials. Moreover, the impedance and phase plots of the FND remained stable for more than 10 000 stretching cycles at a strain of 30% (Figure 2i; Figure S12f, Supporting Information). The impedance, phase, and CSC remained stable for 21 weeks in 37 °C phosphate-buffered saline (PBS) (Figure S12g–i, Supporting Information). Overall, our FNDs exhibited low moduli and motion-insensitive specific impedances as well as high electrical conductivities, making them superior to most neural devices (Figure 2j; Figure S13, Table S4, Supporting Information). These features ensure a dynamically stable device–brain interface, rapid transfer and transmission of neural signals, and effective recording of neurons

which is related to the molar ratio of glycerol. The data are presented as the mean ± s.d., $n = 5$. d) Obtaining gel fibers with moduli ranging from 85 to 605 kPa with different densities of the network. The data are presented as the mean ± s.d., $n = 5$. e) FNDs showing higher conductivity than previous conductive polymer hydrogels ($1^{\#}$: PANI; $2^{\#}$: PEDOT: PSS/PAAc; $3^{\#}$: PEDOT/PVA-HepMA; $4^{\#}$ and $5^{\#}$: PEDOT: PSS; $6^{\#}$: PEDOT/PU). Serial numbers point to references at Table S1 (Supporting Information). The data of the FND is presented as the mean ± s.d., $n = 5$. f) Conductance (G, blue) and G/G_0 (red) of FND remain unchanged during axial stretching. G_0 is the conductance of FND at the initial state. g) FND has the highest CSC amongst most neural devices ($1–4^{\#}$: metal wires; $5–8^{\#}$: carbon-based fibers; $9^{\#}$ and $10^{\#}$: modified metal wires; $11^{\#}$ and $12^{\#}$: modified carbon-based fibers). Serial numbers point to references at Table S2 (Supporting Information). The data of the FND is presented as the mean ± s.d., $n = 5$. h,i) Cyclic voltammogram curves and impedance plots of FNDs at the initial state (before stretching), first and 10 000th cycle of stretching at 30% strain show FND is stable. j) Ashby-style plot comparing modulus (300 ± 25 kPa) and specific impedance (Z_s, 579 ± 78 kΩ) of FND with other neural devices indicate FND performance is superior. Range of values: Metal wire, Z_s: 2.6×10^7–1.2×10^9, modulus: 3.5×10^{10}–6.4×10^{11}; Silicon-based, Z_s: 6.0×10^6–7.0×10^8, modulus: 1.6×10^{11}; Carbon-based, Z_s: 2.3×10^6–2.3×10^8, modulus: 1.1×10^{10}–3.8×10^{11}; Glass-based: Z_s: 2.5×10^6–9.0×10^8, modulus: 9×10^{10}; Polymer-based without network in liquid structure, Z_s: 9.0×10^6–3.4×10^9, modulus: 1.5×10^8–5.0×10^{10}. The impedance shown in (j) includes both ionic conductance and electronic conductance contributions. See Table S4 (Supporting Information) for more details. Measurements (f,h,i) were repeated using five different samples and typical examples are shown.

under intense dynamic deformations with a simultaneously high signal-to-noise ratio, fidelity, and stability.

2.2. FND Records Simulated Neural Signals In Vitro

Before implantation, we conducted the FND by recording the simulated neural signals in an agarose gel with deionized water, a typical in vitro substitute for brain tissue.[26] In freely moving animals or those engaged in vigorous activities, head movements can dynamically deform brain tissues in three dimensions.[27] Signal drift or loss occurs when there is a relative displacement between the neural device and the neuron. To simulate this scenario, the tips of the signal input and the recording devices were placed in contact. A commercial digital neural signal simulator was used to generate simulated neural signals containing local field potentials and spikes (Figure S14, Supporting Information).[28] The signal recording was interrupted if the relative displacement between the devices increased during dynamic shaking (**Figure 3a**). In the experimental group, the FNDs served as both the signal input and recording devices. As a control, we used PtIr wires (≈17 µm in diameter) insulated with parylene (≈1 µm) as non-stretchable recording devices because they are commonly used as commercial fiber devices for chronic recordings owing to their lower modulus (≈100 GPa) compared to other commercial devices based on silicon (≈165 GPa) or tungsten (≈390 GPa). All devices were inserted as a single conductor, and the sensing surface area was the cross-sectional area of the tip.

In the static state, both the PtIr wire and FND could record the simulated signals continuously. However, after 10–20 s of shaking (with the highest acceleration of up to 3.4 ms^{-2} and a frequency over 1 kHz), more than half of the single-unit spikes recorded by the PtIr wire began to disappear and were completely lost after 1 min. The PtIr wire was unable to recover the spike recording, even after the shaking stopped (Figure 3b; Figure S15, Supporting Information). In contrast, FND maintained stable recordings throughout the test process. Furthermore, we found that the interface between the signal input device and the FND within the gel was stable after shaking, whereas the interface with the PtIr wire was separated (Figure 3c,d). Consistent with the finite-element simulations, having a modulus that matched that of the agarose gel prevented FND displacements during shaking (Figure S16, Supporting Information). We also tested the FND and PtIr wire in a static state and replaced the deionized water with PBS in an agarose gel mimicking a fluid environment to verify the intrinsic recording abilities of the FND for high-frequency signals. The average signal-to-noise ratio of single-unit spikes in the FND was approximately three times higher than that in the PtIr wire (Figure S17, Supporting Information).

2.3. FND Records Neural Signals In Vivo

For neural devices to be implantable, they must be biocompatible. To investigate the biocompatibility of the FNDs, we implanted FNDs, PtIr wires, and state-of-the-art flexible neural devices, including carbon fibers and polymer-based flexible devices, into the hippocampi of mouse brains. The immunohistochemistry data were analyzed to evaluate the inflammatory responses after 7 and 21 weeks. FNDs and other flexible neural devices were implanted into mouse brains with the assistance of a rigid tungsten wire, which was withdrawn after the adhesive was dissolved in the cerebrospinal fluid (Figure S18, Supporting Information). The examined inflammation markers included glial fibrillary acidic protein (GFAP) expressed on activated astrocytes and ionized calcium-binding adaptor molecule 1 (Iba1) expressed on microglia. Neurons were identified using NeuN antibodies. Fluorescence images showed that the auxiliary tungsten wire did not induce obvious inflammatory responses immediately after implantation into the brain tissue (Figure S19, Supporting Information). Brains implanted with FNDs had fewer activated astrocytes than those implanted with PtIr wires and were comparable to those implanted with other flexible neural devices after 7 and 21 weeks (Figures S20,S21, Supporting Information). The FND also maintained a small footprint during chronic implantation (Figure S22, Supporting Information). These results indicated good biocompatibility of the FNDs. Furthermore, we demonstrated single-unit tracking in the mouse brain for up to 5 months, demonstrating the stable chronic recording ability of FNDs (Figure S23, Supporting Information).

To test the performance of the proposed FNDs in vivo, we selected the cat as the medium-sized animal for neural recordings. Neural recordings in the visual system have been extensively employed and have greatly improved our understanding of information processing in vivo, with cats being typical model animals in these experiments.[29] In the visual system, the dorsal lateral geniculate nucleus (dLGN) serves as the major subcortical visual information processing center. The dLGN of cats is located in the deep brain (≈12–14 mm under the cortical surface) and has a laminar structure, that is, layers A, A1, and C, along the dorsal-ventral (top to bottom) axis with a total width of 1.2 mm.[30] Each layer in the axial direction is ≈400 µm. Importantly, each individual neuron in the dLGN is driven monocularly, that is, neurons in layers A and C exhibit contralateral eye responses, whereas neurons in layer A1 exhibit ipsilateral eye responses.[30] Thus, in vivo, classification of layer information is possible by examining the monocularly driven visual responses of the recorded neurons. In addition, neurons in the dLGN have a variety of properties, such as ON and OFF responses to light and dark stimuli.[31] Therefore, neural recordings in the dLGN of cats are essential for studying vision, but stable recordings during vigorous activity have not yet been achieved.

To this end, we fabricated tetrodes and bundles with multiple spatially distributed channels using the proposed FNDs. The tetrode was obtained by juxtaposing four individual FNDs, and different tetrodes were assembled and implanted according to the recording requirements. To ensure precise implantation of the FNDs in the deep brains of cats, we used a tungsten device longer than 15 mm as an auxiliary tool. The FNDs were adhered using gelatin, which was dissolved to withdraw the tungsten device after the FNDs were implanted into the target regions. This strategy was verified using agarose gels (Figure S24, Supporting Information).

We first implanted eight tetrodes arranged in a 2×4 array with 100 µm spacing horizontally and vertically into the dLGN of the cat's brain. After the recovery period, the cat was head-fixed and visually stimulated using a light and dark screen (0.3 s interval),

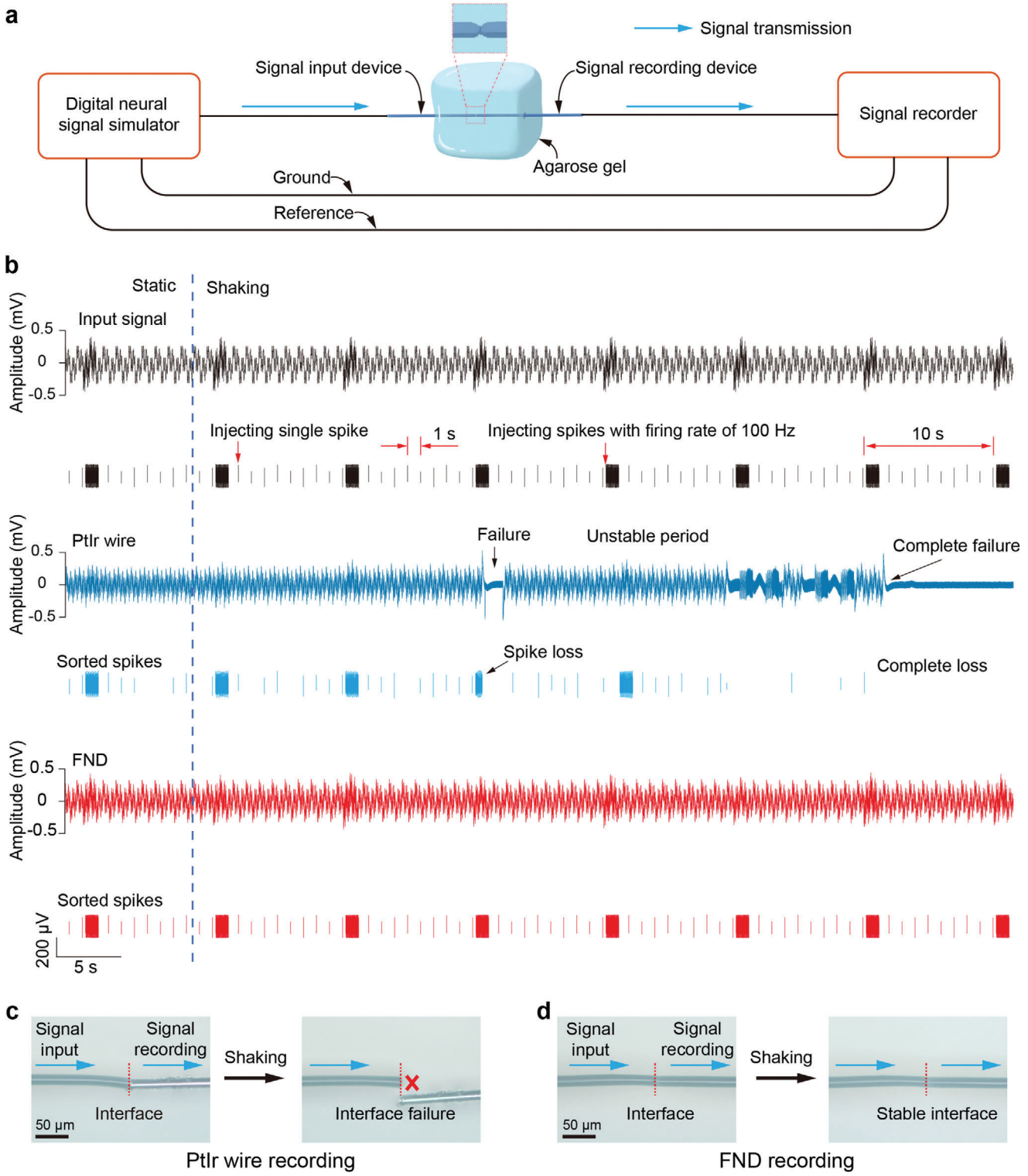

Figure 3. Simulated neural signal recordings in vitro by FND and PtIr wire at dynamic states. a) Schematic showing the simulated neural signal recording by placing devices in agarose gel. Agarose gel was prepared in a rigid plastic container with a size of 10 × 10 × 10 mm. The signal input device was in contact with the signal recording device, and the failure of the interface would lead to the loss of the recorded signal. b) Band-pass filtered waveforms (top) and sorted spikes (bottom) of input and recording signals when gels containing PtIr wire or FND changed from static to shaking states. Soft FND is clearly more reliable at tracking signals than rigid PtIr wire. c,d) Optical microscope images of PtIr wire (c) and FND (d) in agarose gel before and after shaking indicate FND formed and maintained a more stable interface with the signal input device within the gel than PtIr wire did. All measurements were repeated using five independent gels and typical examples are shown.

while neural signals were recorded by these tetrodes (Figure S25, Supporting Information). Six tetrodes effectively captured single-unit spikes. The single-unit spikes recorded by each FND in one tetrode showed the same temporal series, indicating that the four single FNDs tracked the same neuron.

Furthermore, a 16-channel device was formed by bundling 16 FNDs and arranging them longitudinally, with an axial distance of 100 μm between adjacent FNDs. This configuration allowed us to obtain extensive single-unit recordings and enabled signal detection at different locations in the dLGN (Figure S26a, Supporting Information). Neural recordings were performed while visually stimulating the cats with a light and dark screen, with either the left or right eye occluded. Visually evoked responses from neurons were recorded from 12 axially distributed channels with an average of 1.25 single units per recording site. Specifically, Channels 1–4 and 9–12 recorded neurons exhibiting contralateral eye-dominated responses in layers A and C, and Channels 5–8 recorded neurons exhibiting ipsilateral eye-dominated responses in layer A1 (Figure S26b, Supporting Information). Spikes from each neuron were identified according to their distinct waveforms (Figure S26c, Supporting Information), and two single-unit recordings were occasionally identified in one channel (i.e., Channels 1, 2, and 10). The interspike interval (ISI) distributions demonstrated the excellent isolation of single units, as none of the recorded units violated the refractory period, which was defined as <1 ms (Figure S26d–f, Supporting Information).[32]

Finally, we investigated the recording stability of FNDs when the cats performed vigorous activity. One end of the FNDs was implanted into the target brain region, and the other end was connected to a standard adapter that was fixed to the skull. For neural recording under freely moving or running states, the wireless recording system was plugged into the adapter to record neural signals through the FNDs, which were wirelessly transmitted to an external computer without interfering with the cat's activities (Figure S28, Supporting Information). First, we evaluated the effects of vibrations, such as chewing, on signal recording. The results showed that chewing increased background noise but did not affect spike recordings (Figure S27, Supporting Information). The bundle with 16 channels was implanted into the dLGN and connected to a head-attached wireless recording system. Neural recordings were performed when the cat was under freely moving and running states in a homemade transparent running wheel with visual stimuli (**Figure 4**a,b). A head-mounted accelerometer measured the acceleration to determine the possible deformation of the brain tissue.[33] Generally, a higher acceleration value indicates greater brain tissue deformation.[6b,27] For example, when the cats were freely moving, the average and maximum values of the head acceleration along the Y direction were 0.4 and 1 g, respectively. These values increased to 2 and 12 g, respectively, when the cats were running (Figure S29, Supporting Information).

We found that our FNDs could stably track single-unit spikes when the cat changed from a freely moving state to a running state (Movies S3,S4, Supporting Information). Three representative channels are shown in Figure 4. In Channels 1 and 2, spikes of both ON and OFF cells were observed, whereas in Channel 3, only spikes from ON cells were observed. According to standard criteria, ON cells are defined as those responding to light environments, while OFF cells are defined as those responding to dark environments. The ON and OFF cells are randomly distributed in the dLGN.[34] The waveforms, principal component analysis (PCA) results, ON–OFF cell properties, and ISI distributions of these spikes remained stable as the cat changed from a freely moving state to a running state (Figure 4c–n; Figure S30a–c, Supporting Information). Additionally, statistical analysis of the full width at half maximum of the recorded spike waveforms across the 12 channels indicated no significant differences ($P > 0.05$) between the two states (Figure 4o; Figure S30d, Supporting Information). Furthermore, we performed the same neural recordings using other state-of-the-art flexible neural devices, including carbon fiber- and polymer-based devices. The signals recorded in the freely moving state were lost when the cat entered the running state, which may have occurred because the devices were unstretchable and had high moduli (Figure S31, Supporting Information). Finally, the cat implanted with our FNDs was subjected to running three times a day. No signal loss was observed after 100 times of repeated running and freely moving states, demonstrating the long-term recording capability of the FNDs (Figure S32, Supporting Information).

3. Conclusion

In this study, we report an implantable neural device based on soft conductive fibers with a network-in-liquid structure inspired by axons. Highly conductive nanofibers were assembled in a liquid matrix to form a network-in-liquid structure, which solved the intrinsic tradeoffs among low modulus, low specific interfacial impedance, and high electrical conductivity. Instead of simply reducing the dimensions to decrease the bending stiffness, we propose low-modulus materials to make the neural device soft intrinsically. The combination of these properties enables reliable recording of single-unit spikes from the cat brain, even under vigorous activities that inevitably occur and cause significant brain deformations. Such a recording has not been realized previously (Table S4, Supporting Information). The channel count demonstrated here is sufficient for many neurobiological studies, such as those exploring the sustained antidepressant effects of ketamine and brain function during naturalistic behaviors (Table S5, Supporting Information). Our device allows neural recording under various levels of activity that are essential in daily life for animals or humans, offering reliable tools for neurobiological research in complex situations. Our fiber devices complete the neural recording puzzle and have the potential to promote the development of brain science, such as studying the neurophysiology of exercise. Moreover, we believe that the network-in-liquid structure is applicable for designing various bioelectronics that require stable contact with soft tissues, such as fiber biosensors for detecting neurotransmitters in tissues with different moduli, including spinal cords and intestines.

4. Experimental Section

Preparation of FNDs: The 1% PEDOT: PSS suspension solution (PH1000, Heraeus) was added to a glass bottle and placed on a heating stage at 90 °C with continuous shaking every 5 min. Water was evaporated until the concentration reached a solid content of 2.5%. Subsequently, a mixed solution was prepared by adding 5 wt.% DMSO (Sinopharm Chemical Reagent Co., Ltd). The solution was stirred for 2 h and then filtered

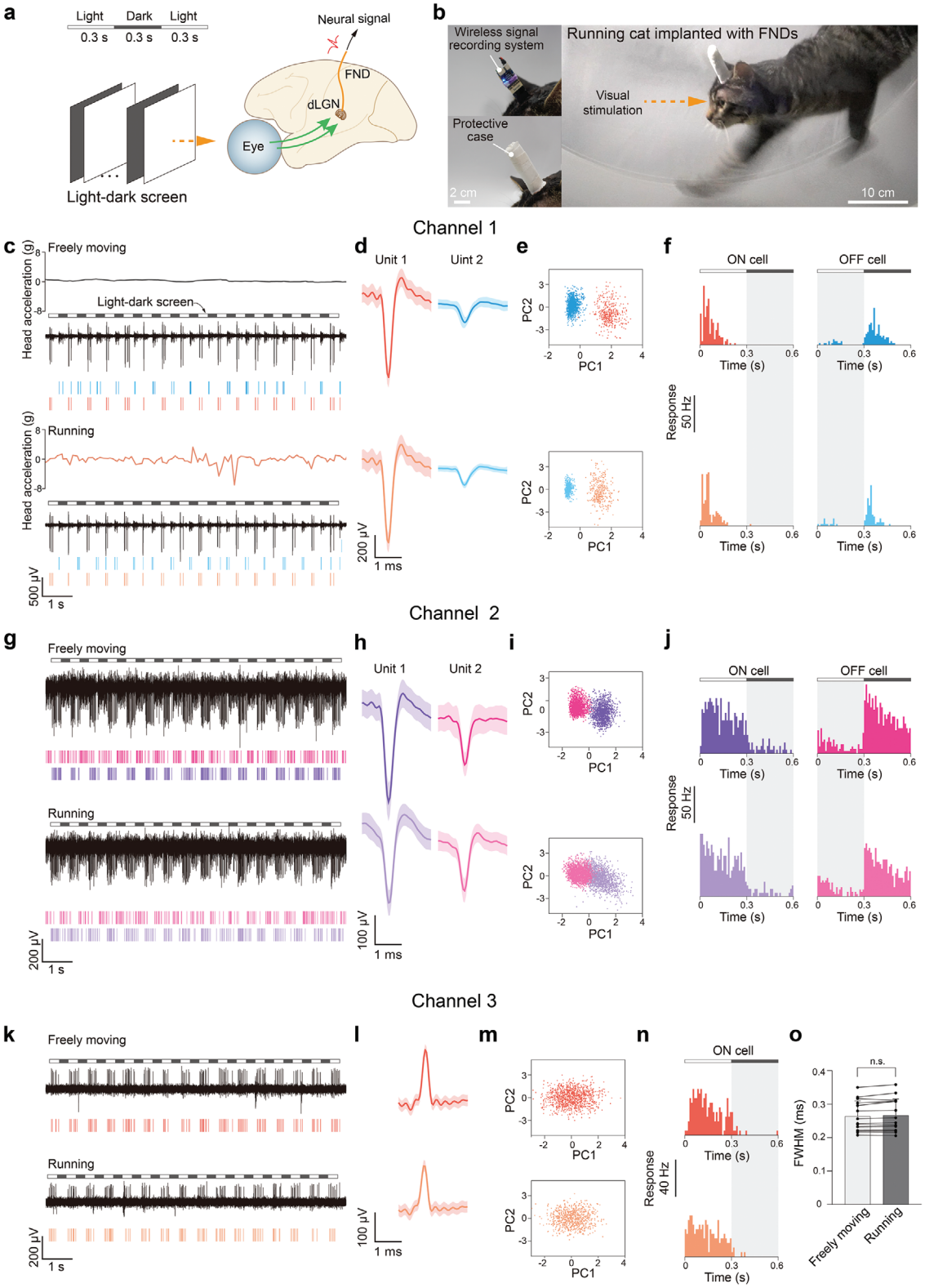

Figure 4. Neural recordings obtained by the FND implanted in the cat brain as the animal performed vigorous activities. a) Schematic showing the FND implanted into the dLGN of a cat for the neural recording of visually evoked responses. b) Photograph of a running cat equipped with a wireless signal recording system connected to an FND for subsequent analysis. c) Conditions and signals of the neural recordings under different states. The curves from top to bottom for the freely moving or running state: head acceleration, visual stimulation marker, band-pass filtered waveforms, and sorted spikes. d) Waveforms of sorted single-unit spikes in c; e) Principal component analysis (PCA) of spikes in (d). f) Analysis of the spikes assigned to ON

through a 0.45-µm syringe filter. Air bubbles were eliminated using vacuum oven treatment at room temperature. For coagulation, a mixture of isopropyl alcohol (IPA, Sinopharm Chemical Reagent Co., Ltd.) and DMSO at a volume ratio of 9:1 was employed. The wet spinning process was conducted using an injection pump (LSP02-2A, Longer Precision Pump Co., Ltd) and 32 G syringe needles at a flow rate of 600 µL min^{-1}. Subsequently, the primary PEDOT: PSS fibers containing IPA and DMSO were immersed in deionized water to ensure the complete removal of IPA and DMSO. The primary PEDOT: PSS fibers were subjected to tension during drying to prevent any reduction in their length. As water evaporated from the fiber, the surface tension and dispersive adhesion caused the networks to collapse, resulting in a rigid fiber. To maintain the network stability, a biocompatible and less volatile liquid matrix (a mixture of glycerol and water) was introduced into the primary fiber through post-infiltration. The infiltration solution was prepared by mixing water and glycerol (Sinopharm Chemical Reagent Co., Ltd.) at molar ratios ranging from 1:1 to 20:1. Gel fibers were obtained by immersing the dry primary fibers in an infiltration solution for 1 h, followed by incubation at room temperature for 4 h. The fluorine rubber was dissolved in 4-methyl 2-pentanone (Sinopharm Chemical Reagent Co., Ltd) and subjected to overnight stirring at a temperature of 80 °C, resulting in the formation of a transparent and viscous solution with a mass fraction of 20%. The gel fiber was immersed in the solution and subsequently withdrawn at a constant velocity while conducting the procedure within a fume hood. The solvent was rapidly evaporated to prevent Plateau–Rayleigh instability. Subsequently, it was suspended in the fume hood for over 24 h to ensure complete solvent evaporation and obtain the FND. For the fluorescence imaging of the insulating layer, coumarin 6 (TCI Shanghai) was dissolved in the solvent.

Morphological and Elemental Characterization: Optical images were acquired using an Olympus EX51. The scanning electron microscopy (SEM) images were obtained with the Zeiss Gemini SEM500 FESEM. Before observing the network structures using SEM, the gel fibers were freeze-dried. Transmission electron microscopy (TEM) images were obtained using a high-contrast transmission electron microscope (HT7800, Hitachi). The X-ray photoelectron spectroscopy (XPS) data were acquired using a scanning XPS microprobe (Thermo Scientific K-Alpha+) equipped with a micro-focused monochromator Al K-alpha X-ray source. A stack of fibers was arranged parallel to the copper tape for XPS testing. The degree of orientation of the gel fibers was characterized by employing small-angle X-ray scattering (SAXS, Xeuss 2.0, Xenocse). Furthermore, the change in intensity with the azimuth angle was determined by integrating the scattering intensity from the 2D scattered pattern.

Modulus Simulation of Gel Fibers Using Finite-Element Method: Finite element analyses were conducted to investigate the mechanical behavior of the fibrous networks with the surrounding liquid matrix. Fibrous networks were generated using the Voronoi method. The initial site points were set randomly in a cubic box, and the Voronoi ridges generated afterward were taken as the edges of the fibrous networks. The volume fraction V_f of the fibrous network in a fiber-matrix composite was calculated as follows:

$$V_f = \frac{l_{fibre} \times A_{fibre}}{V_{cube}} \tag{1}$$

where l_{fibre} represents the total length of the ridge, A_{fibre} represents the cross-sectional area of the fiber, and V_{cube} represents the volume of the cube. The number of initial site points and the size of the cube were adjusted to fit the given volume fraction.

The liquid matrix was simplified as an extremely soft and nearly incompressible material with an embedded fibrous network within it. This treatment ensured that the mechanical behavior of the composites was insensitive to the properties of the matrix. The Young's moduli were set to 9 GPa for the nanofibers forming the fibrous network and 10 Pa for the matrix itself. Accordingly, the Poisson's ratios were 0.3 and 0.48. Embedded coupling between the matrix and fibrous network was adopted, assuming that the latter was deformed in conformity with the surrounding matrix.

The fibrous networks were meshed using 2-node cubic beam elements, and the matrix was meshed using 8-node linear solid elements. A tensile load was applied to the left face of the model, and the right face was pinned. The remaining faces were load-free.

Mechanical Characterization: The stress—strain tests and 180° peeling test were performed using an HY0350 tabletop universal testing instrument.

Electrical and Electrochemical Characterization: The electrical resistance (R) was measured using a Keithley 2410 instrument, while the diameter (d) was determined using an Olympus EX51 microscope, and the length (L) was measured using a Vernier caliper. The FNDs were placed directly on a glass substrate and silver paste was used to establish connections between the fibers and detection probes. The electrical conductivity (σ) was subsequently calculated based on the values of R, d, and L.

$$\sigma = \frac{1}{R} \times \frac{4L}{\pi \times d^2} \tag{2}$$

Electrical Stability under Uniaxial Stretching: A single FND was affixed onto a U-shaped piece of paper with an intermediate spacing of 2 cm, and copper wires were attached to both ends using silver paste. The paper was securely mounted on the HY0350 tabletop universal testing instrument. After confirming that the FND was straightened without any stress, the U-shaped paper was carefully severed. Once the conductance (G) stabilized, it was uniformly elongated at a constant velocity.

Electrochemical Characterization: An electrochemical workstation (CHI660E, CH Instruments, Inc.) was used for the electrochemical characterization. The FND, Ag/AgCl, and platinum wire were used as the working, reference, and counter electrode, respectively. The test was completed by soaking them in PBS (0.01 M, pH = 7.4). Electrochemical impedance spectroscopy was performed using A.C. impedance parameters in the frequency range of 1–100 000 Hz. Cyclic voltammograms were obtained with voltage ranging from −0.6 to 0.8 V with a scan rate of 0.05 V s^{-1}. To assess long-term stability, the FNDs were stored in PBS at 37 °C and tested weekly.

Electrochemical Stability under Dynamic Deformation: Substrates were prepared by pouring the liquid mixture of polydimethylsiloxane (PDMS, Sylgard 184, Dow Corning Co., Ltd) with the elastomer base to the curing agent ratio as 10:1 into a Teflon mold with the size of 70 × 10 × 5 mm (length × width × thickness), and cured at 90 °C for 15 min. The FNDs were subsequently affixed onto these substrates and coated with thin liquid PDMS layers, followed by curing at 50 °C for a duration of 3 h. One end of the FND was attached to a copper wire using silver paste, and the other end was exposed. The substrates were securely mounted onto an HY0350 tabletop universal testing instrument. The electrochemical stability was assessed by comparing the impedance, phase, and cyclic voltammogram (CV) from 0 to 30% strain in the first cycle and the 10 000th cycle under uniaxial stretching.

Recording of Simulated Neural Signal: A commercial digital neural signal stimulator (Blackrock Microsystems) was used. The FND was used to output the simulated neuron signals, and the FND or PtIr wire was used

or OFF cells based on a post-stimulus time histogram. ON cells responded to light (0–0.3 s) and OFF cells responded to dark (0.3–0.6 s). The shadow indicates no response to the visual stimulus. g–j) Representative fragments of band-pass filtered waveforms and sorted spikes (g), waveforms of sorted single-unit spikes (h), PCA results of spikes (i), and analysis of whether the spikes come from ON or OFF cells (j) for Channel 2. k–n) Representative fragments of band-pass filtered waveforms and sorted spikes (k), waveforms of sorted single-unit spikes (l), PCA results of spikes (m), and analysis of whether the spikes come from ON or OFF cells (n) for Channel 3. o) Statistical analysis of the full-width at half-maximum (FWHM) of spikes recorded from 12 channels in the freely moving and running states. n.s., not significant, $P > 0.05$, paired, two-tailed t-test. The histogram indicates the mean ± s.d.

to record the neuron signals. The devices were implanted in a 0.6 wt. % agarose gel with DI water as the solvent for testing, ensuring close contact between their tips. Any change in the relative displacement between the input and recording devices would result in an immediate loss of the signal. The wooden boards were fixed onto a shaker. The agarose gel was prepared in a rigid plastic container with a size of 10 mm × 10 mm × 10 mm, which was subsequently positioned at the distal end of the elongated arm. The headstage was fixed to the container as it was fixed to the skull. Acceleration sensors in the *X*-, *Y*-, and *Z*-directions were integrated into the headstage. The short arm was equipped with a balancing weight, and the agarose gel was carefully placed in a Faraday cage at the opposite end. Signal recording started before the shaker was turned on.

Animals: All mice (ICR, 6 weeks old, male) were purchased from Shanghai SLAC Laboratory Animal Co. Ltd. (certificate number: SYXK-Hu-2022-0012). Normal cats weighing 2.5–3.5 kg were purchased from the Shanghai Jiagan Biotechnology Co. Ltd. (certificate number: SCXK-Hu-2020-0006). Experimental protocols were approved by the Animal Experimentation Committee of Fudan University (certificate number: SYXK-Hu-2020-0032). All animals were treated in accordance with the Guidelines for the Care and Use of Experimental Animals described by the National Institutes of Health and Fudan University.

Immunofluorescence Staining: Animals were euthanized, and their brains were carefully removed. The devices were implanted into the hippocampus of mice. The brain was cryoprotected in 4% paraformaldehyde solution overnight and then sliced into sections with a thickness of ≈4 µm using a microtome (Leica RM2016, Leica Microsystems). Immunofluorescence (IF) staining was performed according to the standard procedures. Typically, antigen retrieval was performed by heating in 0.01 M citrate buffer (pH 6.0) for 8 min at medium heat in a microwave oven (≈400 W) and another 7 min at medium-low heat in a microwave oven (≈240 W) after a break for 8 min.

I. NeuN+GFAP+DAPI

Anti-GFAP (1:1000, GB11096, Servicebio) and anti-NeuN (1:500, GB13138-1, Servicebio) antibodies were used as primary antibodies; Cy3 conjugated goat anti-rabbit IgG (H+L) (1:300, GB21303, Servicebio) and Alexa Fluor 488-conjugated goat anti-mouse IgG (H+L) (1:400, GB25301, Servicebio) were used as secondary antibodies. The IF sections were mounted with DAPI (G1012, Servicebio).

I. NeuN+Iba1+DAPI

The primary anti-GFAP antibodies were replaced with anti-Iba1 antibodies (1:200, GB13105-1, Servicebio). The secondary antibody Cy3-conjugated goat anti-mouse IgG (H+L) was replaced with Cy3-conjugated goat anti-rabbit IgG (H+L) (1:300, GB21303, Servicebio), and the other steps were the same as described in (I). IF sections were observed using Pannoramic MIDI (3DHISTECH Ltd.).

I. Characterization of footprints left by the FND

Tissue Fixation: The mice were deeply anesthetized and transcardially perfused with ice-cold 1× phosphate-buffered saline (PBS), followed by ice-cold 4% paraformaldehyde solution. The dissected samples were incubated in 4% paraformaldehyde at 4 °C with gentle shaking, and washed with 1× PBS for 2 h twice at room temperature.

Tissue Clearing and Immunostaining: The collected samples were processed using the SHIELD method.[35] Before clearing, SHIELD postfixation was applied to the samples according to the manufacturer's instructions. The samples were cleared for several days using SmartBatch clearing mode (LifeCanvas Technologies, USA). After delipidation, the samples were actively immunolabeled using the SmartBatch labeling mode. Each sample was stained with primary antibodies (NeuN, CST 24307S) along with fluorescently conjugated secondary antibodies (Alexa Fluor 647, A21244) in 1:2 (primary: secondary) molar ratios (Jackson ImmunoResearch). After staining, the samples were transferred to EasyIndex (LifeCanvas Technologies, USA) for index matching until the samples were transparent.

3D Tissue Imaging and Image Processing: 3D fluorescence imaging of the cleared tissues was performed using a Nuohai LS 18 Tiling Light Sheet Microscope (Nuohai Life Science (Shanghai) Co., Ltd., Shanghai, China). The laser line was 637 nm. A 3-tile tiling light sheet was used to illuminate the sample.[36] and a 10×/0.6NA objective (Olympus XLPLN10XSVMP) was used to collect the fluorescence. The magnification of the microscope was set at 5×, and the spatial resolution was ≈0.25 × 0.25 × 0.7 μm^3 at the selected imaging conditions. The collected images were processed using the LS 18 ImageCombine software (Nuohai Life Science (Shanghai) Co., Ltd.) and rendered using Amira (Thermo Fisher Scientific, USA).

In Vivo Electrophysiology: FND-based tetrodes and bundles were connected to a 2 × 10 pin connector using silver paste. Each 2 × 10 pin connector connected four tetrodes, and two connectors were used for eight tetrodes. Silicone rubber was used to seal the joints. Five grams of gelatin was added to 10 g of deionized water and was stirred and dissolved at a temperature of 160 °C to form a viscous gelatin solution. Flexible devices were attached to commercial tungsten devices (Kedou BC Co. LTD) using this gelatin solution. Carbon-fiber devices were obtained by insulating bare carbon fibers (Toray Industries, Inc.) with parylene. Polymer-based devices were purchased from Kedou BC.

The surgical procedure commenced with the administration of 5.0% isoflurane for anesthesia induction, followed by maintenance with 2.0–3.0% isoflurane. Additionally, lidocaine was infiltrated into all pressure points, and the tissues were incised to ensure local anesthesia. Craniotomies were performed above the dLGN (Horsley–Clarke coordinates A6, L9), which lay 12–14 mm beneath the cortical surface. The dura was carefully exposed and a plastic tube was positioned over the exposed cortex and secured in place using dental cement. After implantation of the FNDs, the recording chamber was filled with 4% warm agarose in saline and covered with wax to minimize brain pulsation and prevent dehydration. Finally, the connector of the FNDs was firmly fixed to the skull using a dental resin adhesive (Super Bond C&B, SUN MEDICAL) for recordings.

During surgery, the cats were paralyzed using intravenous gallamine triethiodide (8–10 mg k^{-1} g h^{-1}) and artificially respired using a pulmonary pump (catalog #6025, UGO Basile) to maintain end-tidal CO_2 at 3.5–4.0%. Throughout the procedure, the body temperature of the cats was monitored and kept at 38.0 °C by an automatic-feedback-controlled temperature system (BME-461A, Institute of Biomedical Engineering, Chinese Academy of Medical Sciences). Electrocardiography was performed continuously to ensure adequate anesthesia.

For neural recordings under anesthesia, the pupils of the cat were dilated with 1% atropine, the nictitating membranes were retracted with 5% neosynephrine, and contact lenses were used to correct and refract the eyes. The cat's head was fixed on a stereotaxic apparatus and the eyes were kept at the center of the screen. Opaque black paper was used to cover the eyes and identify the dominant eye.

For neural recording under freely moving and running states, the cats were placed in a homemade transparent running wheel after a recovery period of three weeks and became acquainted with the experimental environment.

In all cat experiments, a full-screen flash (0.3 s of light followed by 0.3 s of darkness) was given by a Visual Graphic Systems graphic board (VGS 5, Cambridge Research Systems). Visual stimuli were presented on a CRT monitor (FlexScan F931; Eizo Nanao) refreshing at 100 Hz and positioned ≈57 cm away from the cats' eyes.

In the head-fixed experiments, neural signals were amplified using a microelectrode amplifier (Model 1700, A-M Systems) and collected using an analog-to-digital converter (CED Micro1401, Cambridge Electronic Design Ltd.) to test the dominant eye. Multibundle recording data were collected using the CerePlex Direct (Blackrock Microsystems). In the freely moving and running experiments, the signals were tracked using a wireless recording system (CE32, Beijing Creation-Tech). Spikes were sorted and analyzed using Spike 2 software (version 6, Cambridge Electronic Design) after the recorded signals were bandpass filtered (300–3000 Hz). The ON and OFF cells were analyzed using MATLAB (R2023a, MathWorks). The

head acceleration of the cat was measured using a wireless attitude sensor (WitMotion, Shenzhen Co. Ltd.).

Statistical Analysis: Data was used without pre-processing. Unless otherwise stated, data was shown as means ± s.d. and the sample size was five. Comparisons between the two groups were performed using paired or unpaired two-tailed *t*-tests. Statistical significance was indicated by n.s. ($P > 0.05$), * ($P < 0.05$), ** ($P < 0.01$), *** ($P < 0.001$), and **** ($P < 0.0001$) in the figures and figure legends. Statistical analyses were performed using Microsoft Excel 2021 (Microsoft, USA).

Supporting Information

Supporting Information is available from the Wiley Online Library or from the author.

Acknowledgements

C.T. and Z.H. contributed equally to this work. This work was supported by MOST (2022YFA1203001, 2022YFA1203002), NSFC (T2321003, 22335003, 52122310, 22075050, T2222005, 22175042), and CPSF (2023M740652). The authors thank A.-L. Chun of Science Storylab, Prof. Jue Deng, and Prof. Songlin Zhang for critically reading and editing the manuscript.

Conflict of Interest

The authors declare no conflict of interest.

Data Availability Statement

The data that support the findings of this study are available in the supplementary material of this article.

Keywords

fiber devices, neural recordings, polymer fibers, vigorous activities, visual responses

Received: June 3, 2024
Revised: July 15, 2024
Published online: July 25, 2024

[1] a) A. P. Alivisatos, M. Chun, G. M. Church, K. Deisseroth, J. P. Donoghue, R. J. Greenspan, P. L. McEuen, M. L. Roukes, T. J. Sejnowski, P. S. Weiss, R. Yuste, *Science* **2013**, *339*, 1284; b) C. Xie, J. Liu, T.-M. Fu, X. Dai, W. Zhou, C. M. Lieber, *Nat. Mater.* **2015**, *14*, 1286; c) B. Tian, C. M. Lieber, *Chem. Rev.* **2019**, *119*, 9136; d) B. K. Pedersen, *Nat. Rev. Endocrinol.* **2019**, *15*, 383; e) T. R. Insel, S. C. Landis, F. S. Collins, *Science* **2013**, *340*, 687.

[2] a) T. D. Y. Kozai, N. B. Langhals, P. R. Patel, X. Deng, H. Zhang, K. L. Smith, J. Lahann, N. A. Kotov, D. R. Kipke, *Nat. Mater.* **2012**, *11*, 1065; b) A. Canales, X. Jia, U. P. Froriep, R. A. Koppes, C. M. Tringides, J. Selvidge, C. Lu, C. Hou, L. Wei, Y. Fink, P. Anikeeva, *Nat. Biotechnol.* **2015**, *33*, 277; c) J. J. Jun, N. A. Steinmetz, J. H. Siegle, D. J. Denman, M. Bauza, B. Barbarits, A. K. Lee, C. A. Anastassiou, A. Andrei, Ç. Aydın, M. Barbic, T. J. Blanche, V. Bonin, J. Couto, B. Dutta, S. L. Gratiy, D. A. Gutnisky, M. Häusser, B. Karsh, P. Ledochowitsch, C. M. Lopez, C. Mitelut, S. Musa, M. Okun, M. Pachitariu, J. Putzeys, P. D. Rich, C. Rossant, W.-l. Sun, K. Svoboda, et al., *Nature* **2017**, *551*, 232; d) N. A. Steinmetz, C. Aydin, A. Lebedeva, M. Okun, M. Pachitariu, M. Bauza, M. Beau, J. Bhagat, C. Böhm, M. Broux, S. Chen, J. Colonell, R. J. Gardner, B. Karsh, F. Kloosterman, D. Kostadinov, C. Mora-Lopez, J. O'Callaghan, J. Park, J. Putzeys, B. Sauerbrei, R. J. J. van Daal, A. Z. Vollan, S. Wang, M. Welkenhuysen, Z. Ye, J. T. Dudman, B. Dutta, A. W. Hantman, K. D. Harris, et al., *Science* **2021**, *372*, eabf4588.

[3] a) S. S. Killen, R. Calsbeek, T. D. Williams, *Integr. Comp. Biol.* **2017**, *57*, 185; b) V. Brümmer, S. Schneider, H. K. Strüder, C. D. Askew, *Neuroscience* **2011**, *181*, 150; c) G. L. Ferrari, L. C. Oliveira, T. L. Araujo, V. Matsudo, T. V. Barreira, C. Tudor-Locke, P. Katzmarzyk, *Pediatr. Exerc. Sci.* **2015**, *27*, 380.

[4] a) S. P. Lacour, G. Courtine, J. Guck, *Nat. Rev. Mater.* **2016**, *1*, 16063; b) G. Hong, C. M. Lieber, *Nat. Rev. Neurosci.* **2019**, *20*, 330.

[5] Z. Zhao, H. Zhu, X. Li, L. Sun, F. He, J. E. Chung, D. F. Liu, L. Frank, L. Luan, C. Xie, *Nat. Biomed. Eng.* **2023**, *7*, 520.

[6] a) Y. Cho, S. Park, J. Lee, K. J. Yu, *Adv. Mater.* **2021**, *33*, 2005786; b) Y. Feng, T. M. Abney, R. J. Okamoto, R. B. Pless, G. M. Genin, P. V. Bayly, *J. R. Soc. Interface* **2010**, *7*, 1677; c) P. V. Bayly, T. S. Cohen, E. P. Leister, D. Ajo, E. C. Leuthardt, G. M. Genin, *J. Neurotrauma* **2005**, *22*, 845; d) A. K. Knutsen, A. D. Gomez, M. Gangolli, W.-T. Wang, D. Chan, Y.-C. Lu, E. Christoforou, J. L. Prince, P. V. Bayly, J. A. Butman, D. L. Pham, *Brain Multiphys.* **2020**, *1*, 100015; e) P. Jendritza, F. J. Klein, P. Fries, *Nat. Commun.* **2023**, *14*, 577; f) M. Polanco, S. Bawab, H. Yoon, *Biosensors* **2016**, *6*, 27.

[7] a) S. Salaeh, G. Boiteux, P. Cassagnau, C. Nakason, *Polym. Compos.* **2018**, *39*, 1835; b) L. Shi, T. Zhu, G. Gao, X. Zhang, W. Wei, W. Liu, S. Ding, *Nat. Commun.* **2018**, *9*, 2630.

[8] a) C. Yang, Z. Suo, *Nat. Rev. Mater.* **2018**, *3*, 125; b) B. Yao, S. Wu, R. Wang, Y. Yan, A. Cardenas, D. Wu, Y. Alsaid, W. Wu, X. Zhu, X. He, *Adv. Funct. Mater.* **2022**, *32*, 2109506; c) G. D. Spyropoulos, J. Savarin, E. F. Gomez, D. T. Simon, M. Berggren, J. N. Gelinas, E. Stavrinidou, D. Khodagholy, *Adv. Mater. Technol.* **2020**, *5*, 1900652.

[9] C. Storm, J. J. Pastore, F. C. MacKintosh, T. C. Lubensky, P. A. Janmey, *Nature* **2005**, *435*, 191.

[10] a) M. Khalil, C. E. Teunissen, M. Otto, F. Piehl, M. P. Sormani, T. Gattringer, C. Barro, L. Kappos, M. Comabella, F. Fazekas, A. Petzold, K. Blennow, H. Zetterberg, J. Kuhle, *Nat. Rev. Neurol.* **2018**, *14*, 577; b) D. A. Fletcher, R. D. Mullins, *Nature* **2010**, *463*, 485; c) C. Leterrier, P. Dubey, S. Roy, *Nat. Rev. Neurosci.* **2017**, *18*, 713.

[11] a) J. Isaksson, P. Kjäll, D. Nilsson, N. Robinson, M. Berggren, A. Richter-Dahlfors, *Nat. Mater.* **2007**, *6*, 673; b) Y. Jiang, Z. Zhang, Y.-X. Wang, D. Li, C.-T. Coen, E. Hwaun, G. Chen, H.-C. Wu, D. Zhong, S. Niu, W. Wang, A. Saberi, J.-C. Lai, Y. Wu, Y. Wang, A. A. Trotsyuk, K. Y. Loh, C.-C. Shih, W. Xu, K. Liang, K. Zhang, Y. Bai, G. Gurusankar, W. Hu, W. Jia, Z. Cheng, R. H. Dauskardt, G. C. Gurtner, J. B. H. Tok, K. Deisseroth, et al., *Science* **2022**, *375*, 1411.

[12] D. A. Vecchio, S. H. Mahler, M. D. Hammig, N. A. Kotov, *ACS Nano* **2021**, *15*, 12847.

[13] S. Ertan, C. Kaynak, A. Cihaner, *J. Polym. Sci., Part A-1: Polym. Chem.* **2017**, *55*, 3935.

[14] D. V. Lebedev, A. P. Chuklanov, A. A. Bukharaev, O. S. Druzhinina, *Tech. Phys. Lett.* **2009**, *35*, 371.

[15] N. K. Simha, H. Jin, M. L. Hall, S. Chiravarambath, J. L. Lewis, *J. Biomech. Eng.* **2007**, *129*, 767.

[16] S. Ebnesajjad, R. A. Morgan, *Fluoropolymer additives*, William Andrew, Kidlington, Oxford, UK **2012**.

[17] P. Wang, J. Zhou, B. Xu, C. Lu, Q. a. Meng, H. Liu, *Adv. Mater.* **2020**, *32*, 2003453.

[18] H. Yuk, C. E. Varela, C. S. Nabzdyk, X. Mao, R. F. Padera, E. T. Roche, X. Zhao, *Nature* **2019**, *575*, 169.

[19] a) F. Mirri, N. D. Orloff, A. M. Forster, R. Ashkar, R. J. Headrick, E. A. Bengio, C. J. Long, A. Choi, Y. Luo, A. R. Hight Walker, P. Butler, K. B.

Migler, M. Pasquali, *ACS Appl. Mater. Interfaces* **2016**, *8*, 4903; b) A. de Ryck, D. Quéré, *Langmuir* **1998**, *14*, 1911.
[20] a) D. L. Hunt, C. Lai, R. D. Smith, A. K. Lee, T. D. Harris, M. Barbic, *Nat. Biomed. Eng.* **2019**, *3*, 741; b) G. Schiavone, X. Kang, F. Fallegger, J. Gandar, G. Courtine, S. P. Lacour, *Neuron* **2020**, *108*, 238.
[21] Y. Ohm, C. Pan, M. J. Ford, X. Huang, J. Liao, C. Majidi, *Nat. Electron.* **2021**, *4*, 185.
[22] a) G. Li, K. Huang, J. Deng, M. Guo, M. Cai, Y. Zhang, C. F. Guo, *Adv. Mater.* **2022**, *34*, 2200261; b) X. Wang, S. Zheng, J. Xiong, Z. Liu, Q. Li, W. Li, F. Yan, *Adv. Mater.* **2024**, *36*, 2313845; c) S. Jung, H. W. Choi, F. C. Mocanu, D.-W. Shin, M. F. Chowdhury, S. D. Han, Y.-H. Suh, Y. Cho, H. Lee, X. Fan, S. Y. Bang, S. Zhan, J. Yang, B. Hou, Y. T. Chun, S. Lee, L. G. Occhipinti, J. M. Kim, *Sci. Rep.* **2019**, *9*, 20376.
[23] T. W. McAllister, J. C. Ford, S. Ji, J. G. Beckwith, L. A. Flashman, K. Paulsen, R. M. Greenwald, *Ann. Biomed. Eng.* **2012**, *40*, 127.
[24] C. Boehler, S. Carli, L. Fadiga, T. Stieglitz, M. Asplund, *Nat. Protoc.* **2020**, *15*, 3557.
[25] J. Rivnay, H. Wang, L. Fenno, K. Deisseroth, G. G. Malliaras, *Sci. Adv.* *3*, 1601649.
[26] Z. J. Chen, G. T. Gillies, W. C. Broaddus, S. S. Prabhu, H. Fillmore, R. M. Mitchell, F. D. Corwin, P. P. Fatouros, *J. Neurosurg.* **2004**, *101*, 314.
[27] N. Atsumi, Y. Nakahira, E. Tanaka, M. Iwamoto, *Ann. Biomed. Eng.* **2018**, *46*, 736.
[28] G. K. K. Chik, N. Xiao, X. Ji, A. C. O. Tsang, G. K. K. Leung, S. Zhang, C. Tin, P. K. L. Chan, *Adv. Mater. Technol.* **2022**, *7*, 2200143.
[29] D. H. Hubel, T. N. Wiesel, *J. Physiol.* **1962**, *160*, 106.
[30] T. D. Shou, A. G. Leventhal, *J. Neurosci.* **1989**, *9*, 4287.
[31] S. B. Rompani, F. E. Müllner, A. Wanner, C. Zhang, C. N. Roth, K. Yonehara, B. Roska, *Neuron* **2017**, *93*, 767.
[32] D. S. Reich, F. Mechler, K. P. Purpura, J. D. Victor, *J. Neurosci.* **2000**, *20*, 1964.
[33] P. Saboori, G. Walker, *Ann. Biomed. Eng.* **2019**, *47*, 1982.
[34] J. Z. Jin, C. Weng, C.-I. Yeh, J. A. Gordon, E. S. Ruthazer, M. P. Stryker, H. A. Swadlow, J.-M. Alonso, *Nat. Neurosci.* **2008**, *11*, 88.
[35] Y.-G. Park, C. H. Sohn, R. Chen, M. McCue, D. H. Yun, G. T. Drummond, T. Ku, N. B. Evans, H. C. Oak, W. Trieu, H. Choi, X. Jin, V. Lilascharoen, J. Wang, M. C. Truttmann, H. W. Qi, H. L. Ploegh, T. R. Golub, S. C. Chen, M. P. Frosch, H. J. Kulik, B. K. Lim, K. Chung, *Nat. Biotechnol.* **2019**, *37*, 73.
[36] Y. Chen, X. Li, D. Zhang, C. Wang, R. Feng, X. Li, Y. Wen, H. Xu, X. S. Zhang, X. Yang, Y. Chen, Y. Feng, B. Zhou, B. C. Chen, K. Lei, S. Cai, J. M. Jia, L. Gao, *Cell Rep.* **2020**, *33*, 108349.